Gemini IFU, VLA, and *HST* observations of the OH megamaser galaxy IRAS F23199+0123: the hidden monster and its outflow

C. Hekatelyne,[1]★ Rogemar A. Riffel,[1] Dinalva Sales,[2] Andrew Robinson,[3]
Jack Gallimore,[4] Thaisa Storchi-Bergmann,[5] Preeti Kharb,[6] Christopher O'Dea[3,7]
and Stefi Baum[7,8]

[1]*Departamento de Física, CCNE, Universidade Federal de Santa Maria, 97105-900 Santa Maria, RS, Brazil*
[2]*Instituto de Matemática, Estatística e Física, Universidade Federal do Rio Grande, 96203-900 Rio Grande, Brazil*
[3]*School of Physics and Astronomy, Rochester Institute of Technology, 84 Lomb Memorial Drive, Rochester, NY 14623, USA*
[4]*Department of Physics, Bucknell University, Lewisburg, PA 17837, USA*
[5]*Departamento de Astronomia, Universidade Federal do Rio Grande do Sul, 9500 Bento Gonçalves, 91501-970 Porto Alegre, Brazil*
[6]*National Centre for Radio Astrophysics, Tata Institute of Fundamental Research, S. P. Pune University Campus, Post Bag 3,
Ganeshkhind, Pune 411 007, India*
[7]*Department of Physics and Astronomy, University of Manitoba, Winnipeg, MB R3T 2N2, Canada*
[8]*Center for Imaging Science, Rochester Institute of Technology, 84 Lomb Memorial Drive, Rochester, NY 14623, USA*

ABSTRACT

We present Gemini Multi-Object Spectrograph (GMOS) Integral field Unit (IFU), Very Large Array (VLA), and *Hubble Space Telescope* (*HST*) observations of the OH megamaser (OHM) galaxy IRAS F23199+0123. Our observations show that this system is an interacting pair, with two OHM sources associated with the eastern (IRAS 23199E) member. The two members of the pair present somewhat extended radio emission at 3 and 20 cm, with flux peaks at each nucleus. The GMOS-IFU observations cover the inner $\sim$6 kpc of IRAS 23199E at a spatial resolution of 2.3 kpc. The GMOS-IFU flux distributions in Hα and [N II] λ6583 are similar to that of an *HST* [N II]+Hα narrow-band image, being more extended along the north-east–south-west direction, as also observed in the continuum *HST F814W* image. The GMOS-IFU Hα flux map of IRAS 23199E shows three extranuclear knots attributed to star-forming complexes. We have discovered a Seyfert 1 nucleus in this galaxy, as its nuclear spectrum shows an unresolved broad (full width at half-maximum $\approx$2170 km s^{-1}) double-peaked Hα component, from which we derive a black hole mass of $M_{BH} = 3.8^{+0.3}_{-0.2} \times 10^6$ M$_\odot$. The gas kinematics shows low velocity dispersions (σ) and low [N II]/Hα ratios for the star-forming complexes and higher σ and [N II]/Hα surrounding the radio emission region, supporting interaction between the radio plasma and ambient gas. The two OH masers detected in IRAS F23199E are observed in the vicinity of these enhanced σ regions, supporting their association with the active nucleus and its interaction with the surrounding gas. The gas velocity field can be partially reproduced by rotation in a disc, with residuals along the north–south direction being tentatively attributed to emission from the front walls of a bipolar outflow.

Key words: galaxies: individual: IRAS F23199+0123 – galaxies: ISM – galaxies: kinematics and dynamics.

1 INTRODUCTION

(Ultra)luminous infrared galaxies ([U]LIRGs) are among the most luminous objects in the Universe showing infrared (IR) luminosities of $L_{IR} > 10^{12}$ L$_\odot$. These objects are believed to represent a key stage in the evolution process of galaxies in which tidal torques associated with mergers drive gas into the galaxy core, leading to the feeding/triggering of nuclear starbursts or the fuelling of embedded active galactic nuclei (AGN; e.g. Sales et al. 2015).

These merging systems provide a conducive environment for OH maser emission and approximately 20 per cent of [U]LIRGs contain extremely luminous OH masers, emitting primarily in the 1667 and 1665 MHz lines with luminosities 10^{2-4} L$_\odot$

★ E-mail: hekatelyne.carpes@gmail.com

(Darling & Giovanelli 2002; Lo 2005). The OH megamasers (OHMs) are commonly associated with merging systems, but the environment that produces this phenomenon is still not completely understood. Many OHM hosts present a composite spectrum, showing both AGN and starburst features. A possible explanation for these features is that they originate in a central AGN, contaminated by emission of circumnuclear star-forming regions, as the sampling of the observations usually corresponds to more than 1 kpc at the galaxies. Alternatively, the OHM galaxies could represent a transition stage between a starburst and the eruption of an AGN, as suggested by Darling & Giovanelli (2006).

Considering the above scenario, it becomes relevant to investigate the nature of the gas ionization source of OHM galaxies. In this paper, we present Gemini Multi-Object Spectrograph (GMOS) Integral Field Unit (IFU) observations, Very Large Array (VLA) continuum data, and *Hubble Space Telescope* (*HST*) narrow- and broad-band images of the galaxy IRAS F23199+0123, which is an interacting pair of ULIRGs that presents OHM emission. This galaxy is part of a sample of 15 OHM galaxies, for which we have already *HST* images from a project that has the overall goal of relating the merger state and OH maser properties to AGN and starburst nuclear activity. We have selected targets for IFU observations from the 15 galaxies observed with *HST*, on the basis of the morphology revealed by the images. This paper is a pilot study based on multiwavelength observations, aimed to study the gas kinematics and excitation of one OHM galaxy and that we hope to extend to the whole sample.

IRAS F23199+0123 has a redshift $z = 0.13569$ (Darling & Giovanelli 2006), corresponding to a distance of 558 Mpc for which 1 arcsec corresponds to 2.7 kpc at the galaxy, assuming a Hubble constant of $H_0 = 73 \, \mathrm{km \, s^{-1} \, Mpc^{-1}}$. Its OH maser emission was first detected in the Arecibo survey that observed 52 objects with $0.1 < z < 0.26$ (Darling & Giovanelli 2001). Darling & Giovanelli (2006) used spectroscopic data obtained with the Palomar 5-m telescope with the Double Spectrograph in order to perform an optical spectroscopic study of the properties of the sample of the Arecibo survey and identified the nuclear emission of IRAS F23199+0123 as being due to a Seyfert 2 nucleus, based on emission-line ratios.

Our GMOS-IFU data comprise observations of the central region of the eastern galaxy of the IRAS F23199+0123 pair and our aim is to map the distribution and kinematics of the optical line emitting gas and investigate the excitation mechanism of the nuclear emission. This is the first time that OHM galaxies have been observed with an Integral Field Spectrograph, allowing a two-dimensional look at the gas excitation and kinematics in detail. This paper is organized as follows. Section 2 describes the observations and data reduction procedure, and Section 3 explains the emission-line fitting process and present maps for the emission-line flux distributions and kinematics, as well as the *HST* and VLA radio continuum images, while in Section 4 the results are discussed. Finally, the conclusions of this work are presented in Section 5.

2 OBSERVATIONS AND DATA REDUCTION

2.1 VLA radio continuum data

We observed IRAS F23199+0123 with the Karl G. Jansky Very Large Array (VLA) on 2014 April 20. The observations included *X*-band (8–10 GHz) continuum, *L*-band (1–2 GHz) continuum, and *L*-band spectral line observations of the redshifted OH (1665/1667 MHz) maser lines. The *L*-band and *X*-band observations comprised, respectively, three and one 10-min scans, alter-

nating with 3-min scans of the phase calibrator, J2320+0513. We observed the source 3C 48 in both *X* band and *L* band for flux and bandpass calibration.

The VLA pipeline in CASA (McMullin et al. 2007) was used for data reduction. This includes initial data flagging and phase, flux, and bandpass calibrations. The continuum images were generated using multifrequency synthesis (e.g. Conway, Cornwell & Wilkinson 1990; Rau & Cornwell 2011) with natural weighting and deconvolved using the Cotton–Schwab variant of the CLEAN algorithm (Schwab 1984). Imaging included simultaneous deconvolution of neighbouring radio sources within the primary beam. We applied three rounds of phase-only self-calibration based on CLEAN models for the radio continuum (self-calibration is reviewed by Pearson & Readhead 1984). For the *L*-band continuum image, the restoring beam is $1.69 \times 1.28 \, \mathrm{arcsec^2}$, position angle (PA) = $14°$, and the background rms is $0.024 \, \mathrm{mJy \, beam^{-1}}$. The restoring beam of the *X*-band continuum image is $0.339 \times 0.260 \, \mathrm{arcsec^2}$, PA = $29°$, and the background rms is $0.0093 \, \mathrm{mJy \, beam^{-1}}$. The radio continuum images are presented in Fig. 2.

The spectral line visibilities were continuum subtracted in two steps. First, we produced CLEAN continuum models based on line-free channels, and the CLEAN models were subtracted from the observed visibilities. Second, we removed any residual continuum using the CASA task UVCONTSUB; the continuum was determined by averaging visibility spectra over line-free channels. The continuum-subtracted, spectral line data cube was produced using standard Fourier inversion and CLEAN deconvolution. The expected line width of the 1667 MHz feature is 0.68 MHz (Darling & Giovanelli 2001); therefore, to improve the signal-to-noise ratio, we binned the spectral line data to 0.23 MHz channels (roughly 1/3 line width). The restoring beam of the OH spectral line cube is $1.77 \times 1.36 \, \mathrm{arcsec^2}$, PA $14°$, and the typical background rms for a single 0.23 MHz channel is $0.44 \, \mathrm{mJy \, beam^{-1}}$.

2.2 *Hubble Space Telescope* data

HST images of IRAS F23199+0123 were acquired using the Advanced Camera for Surveys (ACS) with the broad-band filter *F814W*, the narrow-band filter *FR656N*, and medium-band *FR914M* filter as part of a snapshot survey program to observe a sample of OHMGs (Program id 11604; PI: D. J. Axon). The total integration time was 600 s in the broad-band (*I*) *F814W* filter, 200 s in the medium-band filter, and 600 s in the narrow-band Hα *FR656N* filter. The bandpass of the *FR656N* narrow-band filter includes both Hα and [N II] λ6548, 6583 emission lines. We have processed the final images in order to remove cosmic rays using IRAF task LACOS_IM (van Dokkum 2001). The continuum-free Hα+[N II] image of IRAS F23199+0123 was constructed according to the following steps: (i) the count rates of a few stars were obtained in both the medium-band (*FR914M*) and narrow-band (*FR656N*) ramp filter images; (ii) from the count rate ratios the mean scaling factor was computed and applied to the medium-band *FR914M* image; (iii) the scaled *FR914M* image was then subtracted from the narrow-band *FR656N* image. We next visually inspected our continuum subtracted Hα+[N II] image to assure that the residual fluxes of foreground stars were negligible within the uncertainties. This procedure results in typical flux uncertainties of 5–10 per cent (see Hoopes, Walterbos & Rand 1999; Rossa & Dettmar 2000, 2003).

The *HST* images (see Fig. 4) show for the first time that IRAS F23199+0123 is indeed an interacting pair and we have obtained IFS of the eastern member of the par (hereafter IRAS 23199E).

2.3 GMOS IFU data

IRAS 23199E was observed using the GMOS (Hook et al. 2004) IFU (Allington-Smith et al. 2002) as part of the program GS-2013B-Q-86 (PI: D. Sales). Only the eastern nucleus was observed, as it presents a steep continuum flux distribution and with bright guide stars available in the GMOS patrol field. The major axis of the IFU was oriented along PA = 215°, approximately along the major axis of the galaxy. The total on source exposure time was 4800 s divided into four individual exposures of 1200 s each. The observations were performed on 2013 August 29 using the B600 grating with the IFU in the one slit mode, in combination with the *GG455* filter. This set-up resulted in an angular coverage of 5.0×3.5 arcsec^2, covering the spectral region from 450 to 750 nm at a spectral resolution of 1.7 Å, as obtained from the measurement of the full width at half-maximum (FWHM) of typical emission lines of the Ar lamp spectrum used for the wavelength calibration.

The data reduction process was performed using routines of the GEMINI package in the Image Reduction and Analysis Facility (IRAF; Tody 1986, 1993) software and followed the standard procedure of spectroscopic data reduction (Lena 2014). First, we subtracted the bias level from each image, performed flat-fielding and trimming. Then, we applied wavelength calibration to the data using the spectra of arc lamps as references and subtracted the sky emission. Finally, we performed flux calibration using a sensitivity function obtained from the spectrum of the H600 photometric standard star observed during the same night of the object observations.

Finally, data cubes for each individual exposures were created at an angular sampling of 0.1×0.1 arcsec^2, which were then median combined using the IRAF GEMCOMBINE task to obtain the final data cube for the object. The peak of the continuum emission was used as a reference during the mosaicking of the individual data cubes and we used the AVSIGCLIP algorithm for bad pixel/cosmic ray removal. We estimated the angular resolution as 0.85 arcsec from the measurement of the FWHM of the flux distribution of field stars present in the acquisition image of the galaxy. This angular resolution corresponds to ∼2.3 kpc at the galaxy for its adopted distance ($d = 558$ Mpc).

In order to remove noise from the final data cube, we performed a spatial filtering using a Butterworth bandpass filter (Gonzalez & Woods 2002; Menezes, Steiner & Ricci 2014; Menezes et al. 2015) via the IDL routine BANDPASS_FILTER.PRO,[1] which allows the choice of the cut-off frequency (ν) and the order of the filter n. A low value of n (e.g. 1) is close to a Gaussian filter, while a high value (e.g. 10) corresponds to an ideal filter. We used $n = 5$ and $\nu = 0.15$ Ny, chosen by comparing the filtered cube with the original one. For lower values of ν, besides the removal of spatial noise, the filter excludes also emission from the galaxy, while for larger values of ν the filtering procedure is not efficient. The filtering process does not change the angular resolution of the data and all measurements presented in the forthcoming sections were done using the filtered cube.

3 RESULTS

3.1 Hα+[N II] GMOS-IFU spectra

In order to map line fluxes, line-of-sight velocity (V_{LOS}), and velocity dispersion (σ) of the emitting gas, we fitted the emission-line
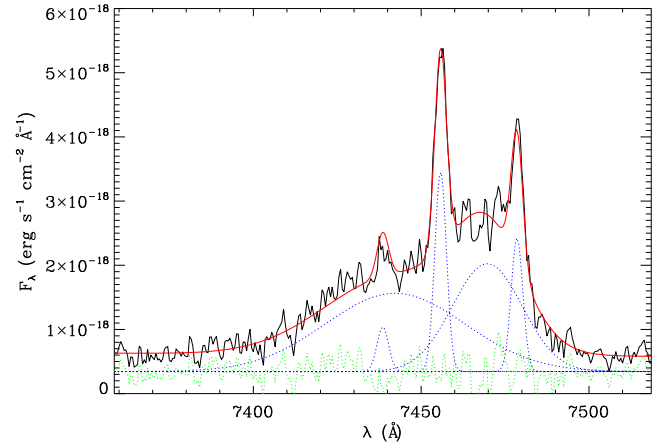
[1] The routine is available at: https://www.harrisgeospatial.com/docs/bandpass-filter.html

Figure 1. Fit of the nuclear spectrum (within 0.8 arcsec from the nucleus) of IRAS 23199E comprising the Hα+[N II] complex. The observed profile is shown in black, while the blue dotted lines represent the broad and narrow components. The red line is the result of the fit, and the green dotted line shows the residual of the fit plus an arbitrary constant.

profiles of Hα and [N II]λλ6548, 6583 with Gaussian curves. The fitting was performed using modified versions of the line-PROfile FITting (PROFIT) routine (Riffel 2010), which provides as outputs the emission-line flux, the centroid velocity, the velocity dispersion and their corresponding uncertainties. Besides the [N II]+Hα emission lines, the nuclear spectrum includes also the [O I] λ6300.3 emission line, which shows a similar profile to that of the [N II] and Hα narrow components, being well reproduced by a single Gaussian curve.

The fitting process for the Hα and [N II] λλ6548, 6583 emission lines was performed simultaneously. We noticed that in the inner 0.8 arcsec radius (corresponding to about two resolution elements), the fitting of a single Gaussian component for each emission line does not reproduce the observed profile, while at larger distances from the nucleus a single component provides a good fit. Thus, at locations farther then 0.8 arcsec from the nucleus (defined as the location of the peak of the continuum emission) we fitted the Hα+[N II] complex using one Gaussian per line, adopting the following constraints: (i) we kept tied the kinematics of the [N II] lines, such that the two lines have the same velocity and velocity dispersion, and (ii) fixed the [N II] λ6583/[N II] λ6548 intensity ratio to its theoretical value (3). The underlying continuum was fitted by a linear function.

Within 0.8 arcsec from the nucleus, we tested two possibilities for the fit to the Hα+[N II] complex. In the first, we fitted the line profiles using four Gaussian curves, in order to include a broad component to represent Hα. The resulting fit does not reproduce the observed profiles adequately. In the second fit, the [N II] lines were fitted by a single Gaussian component, while the Hα profile was fitted by the same narrow component plus two broad components. This procedure resulted in a better fit to the profiles. As the presence of two broad components is restricted to the nucleus and the corresponding emission is not resolved, we propose that they actually represent a single double-peaked line originating in the broad-line region (BLR). Such double-peaked components are not uncommon in AGN (e.g. Storchi-Bergmann et al. 2017).

In Fig. 1 we show the resulting fit of the nuclear spectrum, where the observed profiles are shown in black, the best-fitting model in red and the individual components as dotted blue lines. As the emission of the BLR is not resolved, the width and central wavelength of each broad component and their relative fluxes were kept fixed for
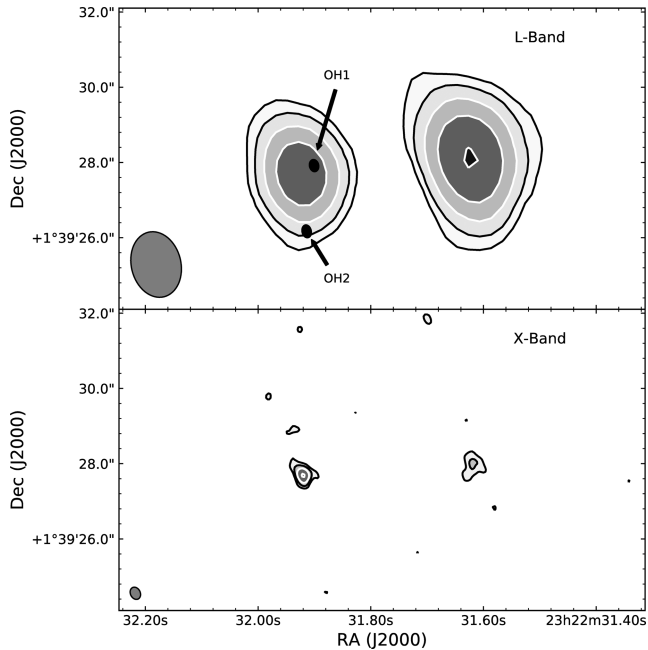
Figure 2. Top panel: VLA *L*-band (1.6 GHz) continuum image of IRAS F23199+0123, shown as filled contours. The contours are (black) 0.071 (3σ), 0.15, (white) 0.32, 0.69, and 1.5 mJy beam^{-1}. The OH1 and OH2 labels identify the locations where the OH maser sources were detected (see Fig. 3). Bottom panel: VLA *X*-band (8 GHz) continuum image of IRAS F23199+0123, shown as filled contours. The contours are (black) 0.0278 (3σ), 0.0647, (white) 0.150, and 0.349 mJy beam^{-1}.

all spaxels, while their amplitudes were allowed to vary to enable for smearing by the seeing. The values of the centroid velocities and velocity dispersions were obtained by fitting an integrated spectrum of the inner 0.8 arcsec. The centroid velocities relative to the systemic velocity are -416 and 668 km s^{-1} for the blueshifted and redshifted components, respectively. The corresponding velocity dispersions are $\sigma = 955$ km s^{-1} for the blue component and $\sigma = 475$ km s^{-1} for the red component. In the hypothesis described above that these two components represent a single double-peaked line, this line profile has a FWHM of 2170 km s^{-1}. The systemic velocity adopted in this paper is $v_s = 37\,947 \pm 2$ km s^{-1} (corrected for the heliocentric rest frame), as derived by the modelling of the gas velocity field as discussed in Section 4.3.

3.2 OH maser spectra

Fig. 3 shows the VLA OH spectra extracted at the positions of the eastern (IRAS 23199E) and western nuclei. OH masers are detected only towards the eastern nucleus. Two line features appear in the spectrum, which we label 'OH1', detected at 5.4σ significance, and 'OH2', a 4.1σ detection. To within the measurement uncertainties, OH1 matches the central frequency and peak flux density of the maser feature detected by Darling & Giovanelli (2001). To our knowledge, OH2 has never been detected before; OH2 falls outside the bandpass of the Darling & Giovanelli (2001) Arecibo observations. The position of OH1 and OH2 defections is identified in the top panel of Fig. 2.

Fig. 3 shows that OH1 appears to identify with the 1665 MHz line at the redshift of the eastern nucleus. Assuming OH1 is indeed the 1665 MHz line, its centroid velocity would be $v = +85 \pm 28$ km s^{-1} relative to systemic in the rest frame of the eastern nucleus. OH2
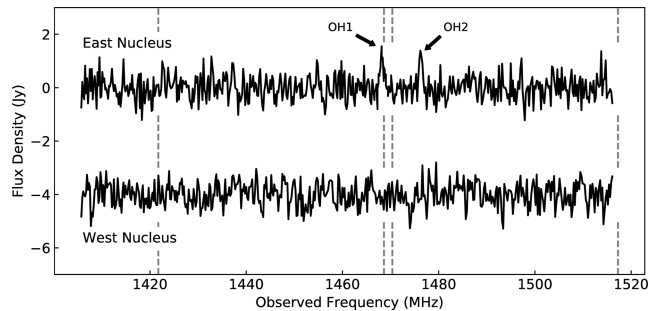

Figure 3. VLA OH maser spectra of the eastern (top) and western (bottom, offset by -4 mJy) nuclei. The vertical, dashed grey lines mark the expected, redshifted frequencies for the 1612, 1665, 1667, and 1712 MHz maser features. Two spectral features are detected at the position of the eastern nucleus, marked OH1 and OH2. OH1 was originally detected by Darling & Giovanelli (2001); OH2 is a new detection.

is however significantly offset from the expected heliocentric frequencies of possible emission lines. It may identify either with 1665 MHz line at $v = -1557 \pm 22$ km s^{-1} or the 1667 MHz line at $v = -436 \pm 29$ km s^{-1} relative to systemic.

3.3 *HST* images

Fig. 4 presents the *HST* broad-band continuum *F814W* image (top panel) and the narrow-band Hα+[NII] image (bottom panel) of the inner 20×20 arcsec^2 of IRAS F23199+0123, which reveal that this system is an interacting pair. The images in the left-hand panels show both galaxies of the pair, while the right-hand panels show a zoomed in view of IRAS 23188E within the same field of view of the GMOS IFU observations. The green box in the left-hand panels corresponds to the field of view of our GMOS data. The *HST* images were rotated to the same orientation of the GMOS data.

The *F814W* continuum image of IRAS 23199E presents the highest intensity levels in an elongated structure at PA ≈ 45° suggesting that the galaxy is highly inclined. The western galaxy of the pair shows a less elongated flux distribution, suggesting a more face-on orientation, although the flux distribution towards the centre is not uniform, but presents a complex structure. The *F814W* image also reveals a structure that resembles a spiral arm to the north that seems to connect the two galaxies, which may be a tidal tail connecting the two galaxies. The linear distance between the galaxy nuclei, projected in the plane of the sky is 24 kpc, assuming a distance to the galaxy of 558 Mpc. This is a lower limit as we do not know the orientation of the plane containing both galaxies or their nuclei relative to the plane of the sky.

The bottom left-hand panel of Fig. 4 shows the continuum-free *HST* Hα+[N II] narrow-band image of the two galaxies. The bottom right-hand panel shows a zoom of the region observed with GMOS-IFU, covering the central part of IRAS 23199E. The Hα+[N II] flux distribution is similar to that of the continuum, and suggests the presence of two tidal tails, one to the north-east and another to the south-west of the nucleus.

3.4 Emission-line flux distributions

The top panels of Fig. 5 present the flux distributions in the narrow components of Hα (left) and [N II] λ6583 (right) emission lines. The colour bars show the flux in logarithmic units of erg s^{-1} cm^2, and the grey regions represent masked locations where the uncertainty
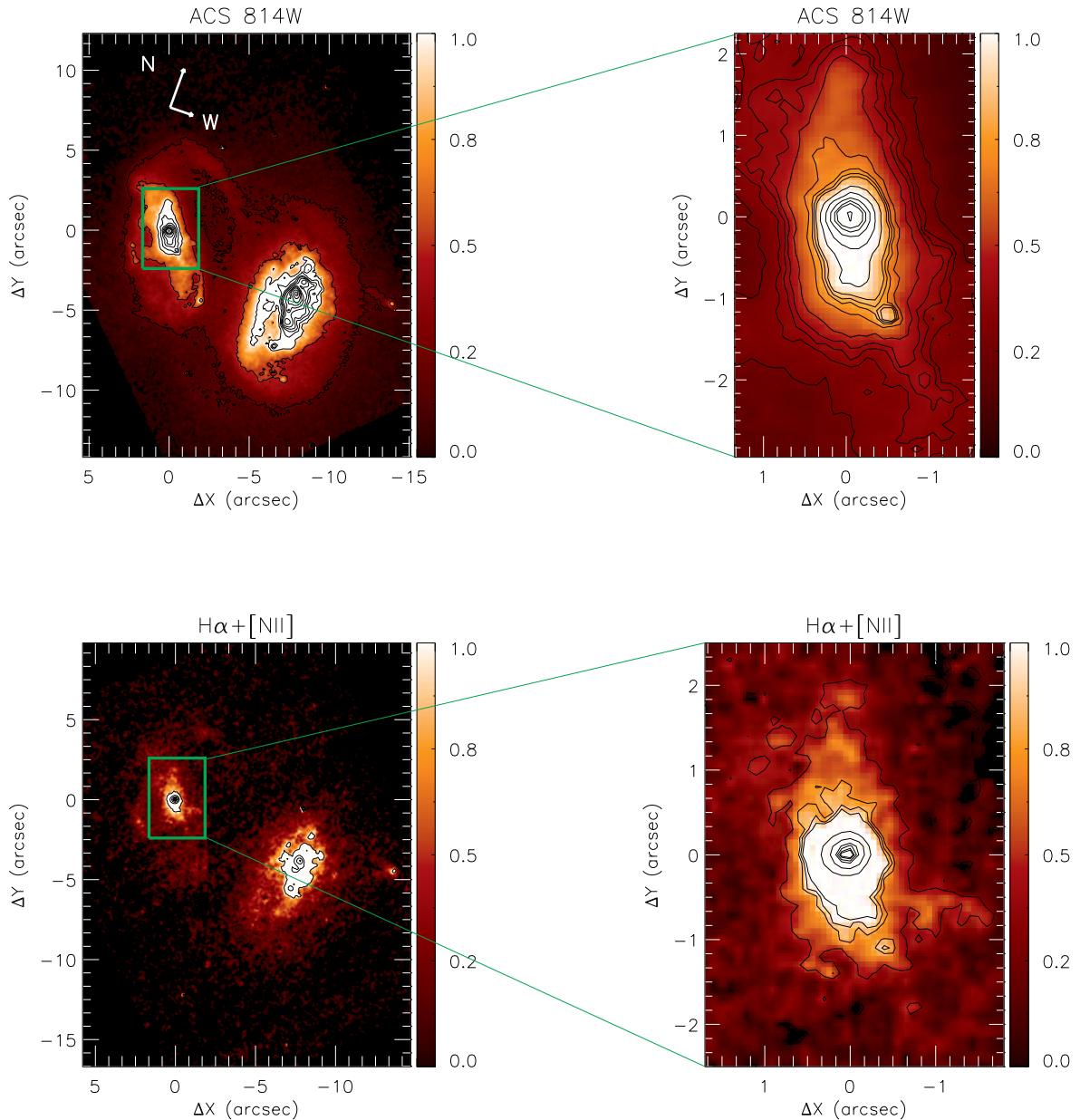
Figure 4. Top panels: left – large-scale image (ACS/*HST F814W* – *i* band); right – zoom of the region observed with GMOS. Bottom panels: left – *HST* large-scale continuum-free Hα+[N II] image; right – zoom at the region observed with GMOS IFU. The green boxes show the GMOS IFU field of view (3.5 × 5.5 arcsec²) and the colour bars show the fluxes in arbitrary units.

in the flux is larger than 30 per cent. The central cross marks the location of the nucleus, defined as the position of the peak of the flux distribution of the broad Hα component and is labelled with the letter N in Fig. 5. The two lines show similar flux distributions, with the emission within the inner ∼1 arcsec being elongated in the north-east–south-west direction. At least three extranuclear knots of emission, labelled A, B, and C in Fig. 5, are observed in the Hα flux map, at (*x*, *y*) angular distances relative to the nucleus of (−0.6, −2.2 arcsec), (−1.0, 1.8 arcsec), and (1.0, −0.6 arcsec). We note that these knots are not observed in the *HST* [N II]+Hα image.

3.5 Gas velocity fields and velocity dispersion maps

The central panels of Fig. 5 present the line-of-sight velocity (V_{LOS}) fields for the Hα (left) and [N II] λ6583 (right) emission lines. White

regions were masked following the same criteria used for the flux maps, described above. The systemic velocity of $V_s = 37\,947\,\text{km s}^{-1}$ was subtracted from the observed velocities, as derived from the modelling of the Hα velocity field with a rotating disc model (see Section 4.3).

The velocity fields derived from Hα and [N II] emission lines are similar, presenting redshifts to the west and blueshifts to the east of the nucleus with velocities reaching up to 200 km s⁻¹. The zero velocity line presents an S-shape and values close to the systemic velocity are observed at ∼2 arcsec to the north of the nucleus.

The bottom panels of Fig. 5 show the velocity dispersion (σ) maps for Hα (left) and [N II] λ6583 (right), corrected for the instrumental broadening. These maps show values ranging from ∼40 to 150 km s⁻¹, with the highest values observed cospatially with the S-shaped zero velocity curve of the V_{LOS} maps (central panels). In
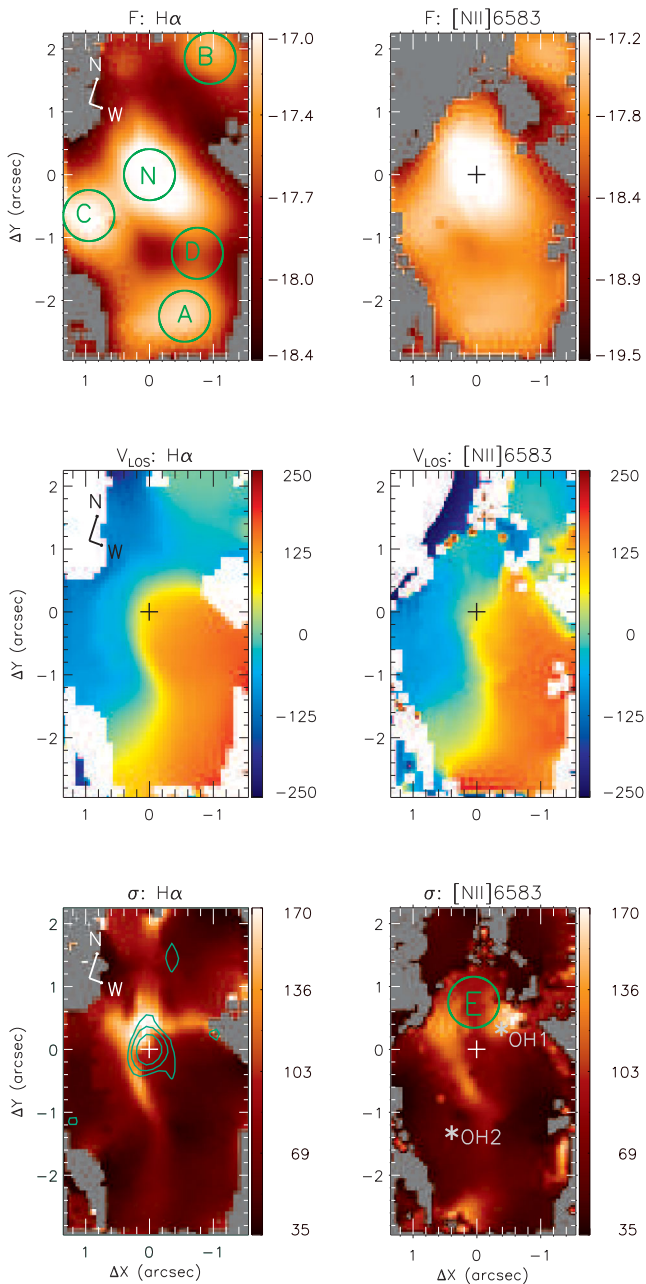
Figure 5. Top panels: flux maps in the Hα (left) and [N II] λ6583 (right) emission lines. The colour bars show the fluxes in logarithmic units of erg s^{-1} cm^{-2}. Central panels: line-of-sight velocity fields for the Hα (left) and [N II] (right) emitting gas. The colour bars show the velocities in units of km s^{-1}, after the subtraction of the systemic velocity of the galaxy. Bottom panels: velocity dispersion maps for the Hα (left) and [N II] (right) emission lines, corrected for the instrumental broadening. The colour bars show the σ values in units of km s^{-1}. The central cross in all panels marks the position of the nucleus and grey regions in the flux and σ maps and white regions in the V_{LOS} maps represent masked locations, where the signal-to-noise ratio was not high enough to obtain reliable fits to the emission-line profiles or locations with no line detection. The green contours in the velocity dispersion map of Hα line are from the 3-cm radio image. The grey asterisks labelled as OH1 and OH2 mark the locations where the maser emission has been detected.
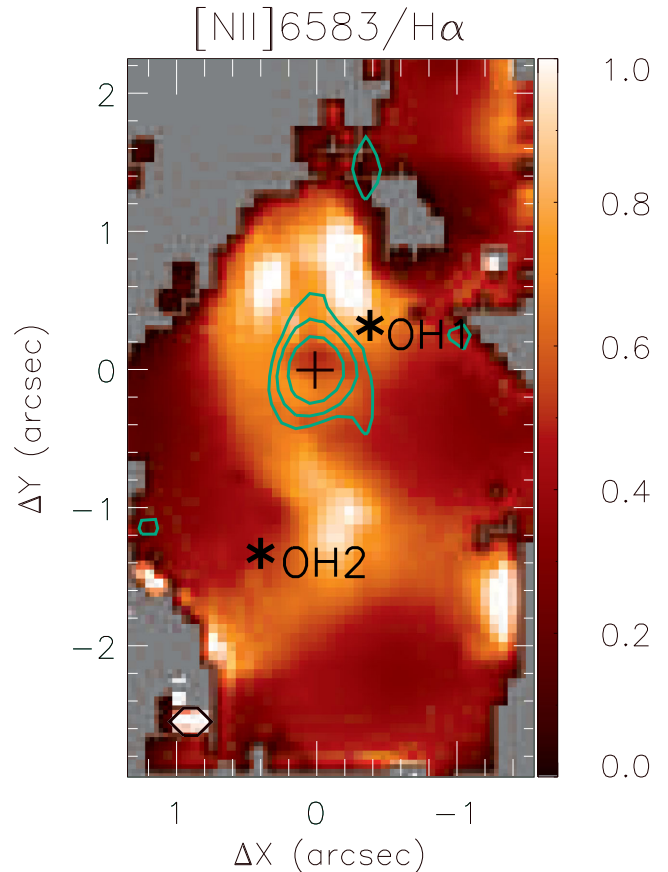

Figure 6. [N II]/Hα flux ratio map for IRAS 23199E. Grey regions correspond to masked locations where no reliable measurements are available. The green contours in the map are from the 3-cm radio image. The black asterisks labelled as OH1 and OH2 mark the position of the maser emission.

addition, some high σ values are seen for Hα at 1.5 arcsec northeast of the nucleus, where the velocity fields present the highest blueshifts. The smallest values of σ are cospatial with the extranuclear knots of emission observed in the emission-line flux distributions in the top panels of Fig. 5.

4 DISCUSSION

In this work, we present for the first time high-quality *HST* images of IRAS F23199+0123. These images allowed us to identify that this system is indeed composed by two members and discern tidal structures. Thus, this is the first time that this system has been established to be an interacting galaxy pair.

4.1 Gas excitation and diagnostic diagrams

The [N II] λ6583/Hα flux ratio can be used to map the gas excitation (e.g. Baldwin, Phillips & Terlevich 1981; Cid Fernandes et al. 2010), with values [N II] λ6583/Hα ≤ 1 corresponding to gas ionized by young stars, while larger values correspond to gas excited by a central AGN or shocks (e.g. Storchi-Bergmann et al. 2007; Cid Fernandes et al. 2011).

In Fig. 6 we present the [N II] λ6583/Hα ratio map for IRAS 23199E. Grey regions correspond to locations masked due to poor fits. The map shows values ranging from ∼0.2 to 1, with the highest values observed approximately coincident with the region with the highest σ values (bottom panels of Fig. 5), while the
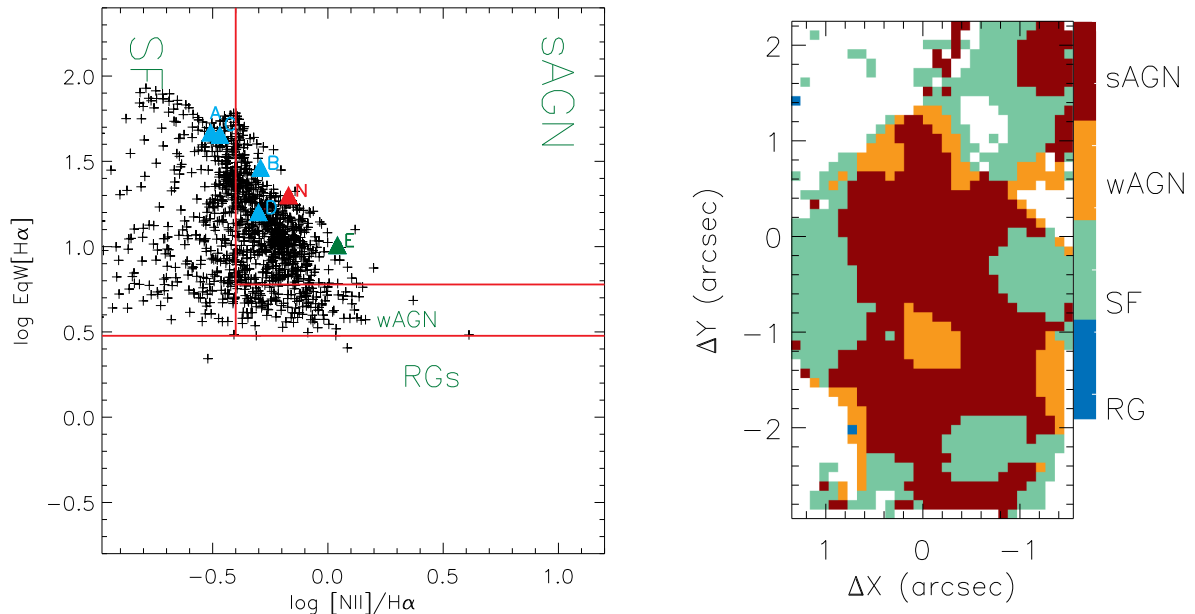
Figure 7. Left: the WHAN diagram for IRAS 23199E showing the different excitation regions (Cid Fernandes et al. 2010). Each cross corresponds to an individual spaxel of the IFU data cube; the red triangle represents the nucleus; blue triangles are for regions A, B, C, and D identified in the Hα flux map of Fig. 5; and the green triangle corresponds to the region E identified in the [N II] σ map of Fig. 5. Right: excitation map identifying the regions within the field of view corresponding to different excitation mechanisms: strong AGN (sAGN), weak AGN (wAGN), star-forming (SF), and retired galaxy (RG).

lowest values are observed in the knots of enhanced Hα emission (top left-hand panel of Fig. 5). We interpret these latter locations as complexes of star-forming regions.

The fact that the locations with the highest [N II] λ6583/Hα ratios are cospatial with the highest σ values suggests that shocks contribute to the gas excitation. We have extracted a spectrum within a circular aperture of 0.4 arcsec radius in one of these locations, labelled E in Fig. 5. We have measured the line ratios and equivalent width of Hα from this spectrum, to plot this region in the diagnostic diagram WHAN (Cid Fernandes et al. 2010). This diagram has been proposed as an alternative to the BPT diagrams of Baldwin et al. (1981), and is a plot of the Hα equivalent width against the [N II] λ6583/Hα flux ratio. While BPT diagrams need four emission lines to separate the regions ionized by AGN or starburst, the WHAN diagram requires just Hα and [N II]. The WHAN diagram enables a separation between starbursts, Seyfert galaxies (sAGN) and low-luminosity AGNs (wAGN). It is also possible to separate wAGN population, where the emitting gas is excited by a central AGN from retired galaxies (RG), where the gas emission may be due to excitation by hot, evolved (post-asymptotic giant branch – post-AGB) stars, in which case the Hα equivalent width is smaller than 3 Å (e.g. Belfiore et al. 2016; Brum et al. 2017).

The WHAN diagram for IRAS 23199E is shown in the left-hand panel of Fig. 7, while the right-hand panel of this figure shows the corresponding excitation map, with the distinct excitation classes identified. The red triangle represents the nucleus, as obtained from the fitting of the line profiles from an integrated nuclear spectrum within 0.4 arcsec radius. Although the Hα broad component is seen to up to 0.8 arcsec from the nucleus – due to the wings of the point spread function (PSF), the smaller aperture of 0.4 arcsec was chosen here to focus on the AGN emission, most of which is contained within this aperture (the PSF FWHM measured from field stars flux distribution is 0.85 arcsec). The blue triangles correspond to the extranuclear locations identified in Fig. 5. The green triangle corresponds to the spectrum from region E described above where there

is an enhancement of both the line ratio and the velocity dispersion σ. All points are located within the region expected for emission of gas excited by an AGN or starburst. In particular, the point corresponding to the nucleus is clearly located within the sAGN region (strong AGN), indicating that the nuclear emission originates in a Seyfert-type AGN, in agreement with the presence of the broad Hα component. In addition to the nucleus, region E can also be classified as sAGN. At this location, the [N II] λ6583/Hα ratio is even larger than for the nucleus, possibly that shocks contribute to the gas excitation. The blue triangles corresponding to the extranuclear regions identified in Fig. 5 are located very close to the line that separates starburst from sAGN excitation, indicating that both the central AGN and star-forming regions contribute to the gas excitation at these locations.

We note that there is a general trend for higher [N II] λ6583/Hα to be associated with larger σ values. Some of these regions surround the contours of the 3-cm radio emission, as shown in Fig. 6. We thus attribute the gas emission at high-σ and [N II]/Hα ratio as at least being partly produced by excitation of the gas by shocks associated with produced by the radio-emitting plasma. There are also some regions to the south of the nucleus where there is no radio emission but there is still enhancement of the σ and line ratios, which we attribute to the presence of additional perturbations possibly due to the interaction between the two galaxies in IRAS F23199+0123.

4.2 Star-forming regions

As discussed in previous sections, we identify several knots of enhanced Hα emission, associated with star-forming regions. These knots are labelled A, B, and C in Fig. 5. In order to characterize the star formation at these locations, we use the integrated fluxes within the circular apertures shown in Fig. 5. These fluxes have been used to estimate physical properties of the star-forming regions that are

Table 1. Physical properties of the star-forming regions in IRAS 23199E.

Region	$L_{H\alpha}$ (10^{41} erg s^{-1})	EqW [Hα]	M (10^5 M$_\odot$)	log Q[H$^+$] (s^{-1})	SFR (M$_\odot$ yr^{-1})
A	0.12	44.41	3.06	52.10	0.09
B	0.07	28.41	1.78	51.87	0.05
C	0.16	45.84	4.08	52.23	0.12

listed in Table 1. In order to estimate the mass of ionized gas we used (Peterson 1997)

$$\frac{M}{M_\odot} \approx 2.3 \times 10^5 \frac{L_{41}(H\alpha)}{n_3^2}, \tag{1}$$

where $L_{41}(H\alpha)$ is the Hα luminosity in units of 10^{41} erg s^{-1} and n_3 is the electron density (N_e) in units of 10^3 cm^{-3}. We have assumed $N_e = 300$ cm^{-3}, which is the mean value of electron density of circumnuclear star-forming regions derived from the [S II] λ 6717/λ 6731 intensity ratio (Díaz et al. 2007; Dors et al. 2008). The values of the mass of ionized gas for each star-forming complex are in the range (1.78–4.08) × 10^5 M$_\odot$.

We estimated the rate of ionizing photons Q[H$^+$] and star formation rate (SFR) under the assumption of a continuous star-forming regime. The rate of ionizing photons for each star-forming region was derived using Osterbrock (1989)

$$Q[H^+] = \frac{\alpha_B L_{H\alpha}}{\alpha_{H\alpha}^{EFF} h \nu_{H\alpha}}, \tag{2}$$

where α_B is the hydrogen recombination coefficient to all energy levels above the ground level, $\alpha_{H\alpha}^{EFF}$ is the effective recombination coefficient for Hα, h is the Planck constant, and $\nu_{H\alpha}$ is the frequency of the Hα line. Using $\alpha_B = 2.59 \times 10^{13}$ cm^3 s^{-1} and $\alpha_{H\alpha}^{EFF} = 1.17 \times 10^{-17}$ cm^3 s^{-1} (Osterbrock 1989) we obtain

$$\left(\frac{Q[H^+]}{s^{-1}} \right) = 1.03 \times 10^{12} \left(\frac{L_{H\alpha}}{s^{-1}} \right). \tag{3}$$

The SFR was computed using the following relation (Kennicutt 1998):

$$\frac{SFR}{M_\odot \, yr^{-1}} = 7.9 \times 10^{-42} \frac{L_{H\alpha}}{erg \, s^{-1}}. \tag{4}$$

SFRs derived for the star-forming regions of IRAS 23199E are in the range 0.05–0.12 M$_\odot$ yr^{-1}, consistent with a moderate star-forming regime. These SFRs fall within the range observed for circumnuclear star-forming regions in nearby Seyfert galaxies, derived using optical (Dors et al. 2008) and near-IR (Falcón-Barroso et al. 2014; Riffel et al. 2016) emission lines and are consistent with the average value of SFR = 0.14 M$_\odot$ yr^{-1} for a sample of 385 galaxies.

The values of the ionizing photons rate are in the range log Q[H$^+$] = (51.87–52.23) s^{-1} and are in agreement with previous reported values for circumnuclear star-forming regions in nearby galaxies (e.g. Wold & Galliano 2006; Galliano & Alloin 2008; Riffel et al. 2009, 2016).

The masses of ionized gas derived for the star-forming complexes in IRAS F23199E are in the range of (1.78–4.08) × 10^5 M$_\odot$, and agree with those previously obtained for star-forming regions surrounding Seyfert nuclei (e.g. Riffel et al. 2016).

We can also use the far-infrared (FIR) luminosity of galaxy to calculate the SFR (Kennicutt 1998):

$$SFR(M_\odot \, yr^{-1}) = 4.5 \times 10^{-44} L_{FIR} (erg \, s^{-1}), \tag{5}$$

where L_{FIR} is the IR luminosity integrated over the mid- and far-IR spectrum (8–1000 μm). Using $L_{FIR} = 1.35 \times 10^{11}$ erg s^{-1} (Darling & Giovanelli 2006), we obtain SFR ≈ 61 M$_\odot$ yr^{-1}. This value is much higher than those obtained for each star-forming region (shown in Table 1) and suggests that most of the FIR luminosity may not be due to star formation, but to the AGN, or most of the star formation is embedded in dust.

4.3 Gas kinematics

The velocity fields shown in Fig. 5 are complex, but they suggest the presence of a rotation pattern with the line of nodes oriented approximately along the east–west direction. In order to describe analytically this behaviour, we used a simple rotation model (van der Kruit & Allen 1978; Bertola et al. 1991), which assumes that the gas moves in circular orbits in the plane of the galaxy, within a central gravitational potential. In this model, the rotation velocity field is given by

$$V_{mod}(R, \psi) = v_s$$
$$+ \frac{AR \cos(\psi - \psi_0) \sin(i) \cos^p(i)}{\{R^2[\sin^2(\psi - \psi_0) + \cos^2(i) \cos^2(\psi - \psi_0)] + c_0^2 \cos^2(i)\}^{\frac{p}{2}}}, \tag{6}$$

where R and ψ are the coordinates of each pixel in the plane of the sky, v_s is the systemic velocity of the galaxy, A is the velocity amplitude, ψ_0 is the major axis position angle, i is the disc inclination relative to the plane of the sky ($i = 0$ for face-on disc), p is a model fitting parameter (for $p = 1$ the rotation curve at large radii is asymptotically flat while for $p = 3/2$ the system has a finite mass), and c_0 is a concentration parameter, defined as the radius where the rotation curve reaches 70 per cent of its velocity amplitude.

The [N II] and Hα emission lines present similar velocity fields (Fig. 5), so we have chosen the Hα velocity field to perform the fit, as this line is stronger than [N II] λ6583 at most locations.

The observed velocities were fitted with the equation above using the MPFITFUN routine (Markwardt 2009) in IDL,[2] which performs a non-linear least-squares fit, after initial guesses for the parameters. During the fit, the position of the kinematical centre was kept fixed to the position of the peak of the flux distribution of the broad Hα component, adopted as the location of the nucleus of the galaxy and the parameter p was kept fixed at $p = 1.5$, as done in previous works (e.g. Brum et al. 2017).

The resulting best-fitting model is shown in the central panel of Fig. 8 and its parameters are $A = 349 \pm 26$ km s^{-1}, $v_s = 37\,947 \pm 2$ km s^{-1} (corrected for the heliocentric rest frame), $\psi_0 = 95° \pm 2°$, $c_0 = 1.6 \pm 0.1$ arcsec, $i = 41° \pm 6°$. The systemic velocity of the galaxy can be compared with previous measurements.

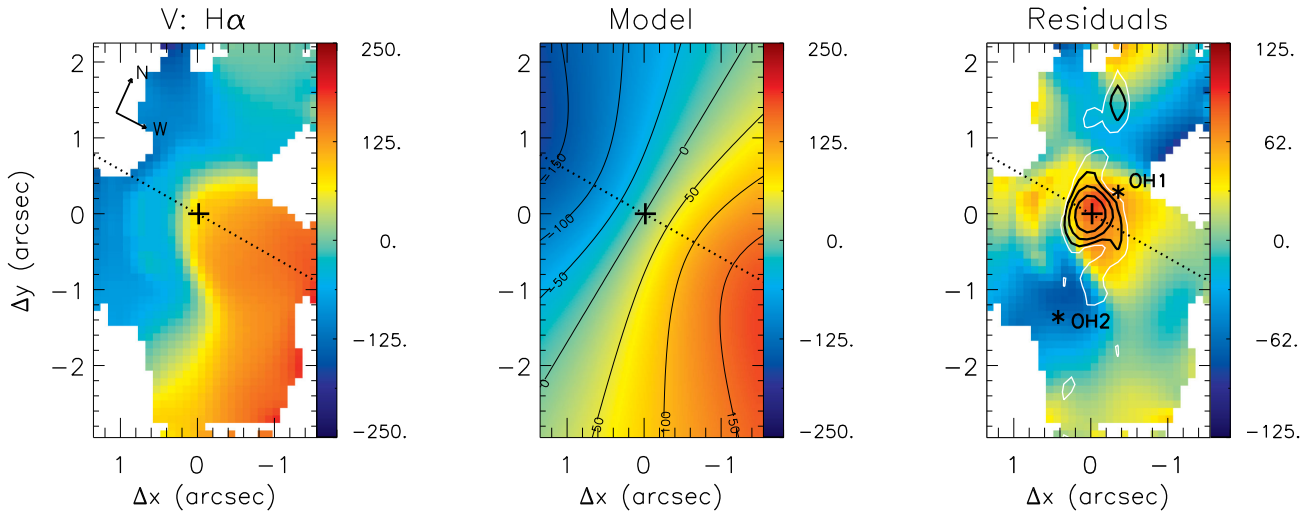[2] http://www.harrisgeospatial.com/ProductsandSolutions/Geospatial Products/IDL.aspx

Figure 8. Observed Hα velocity field (left), rotating disc model (centre), and residual between the two (right). The central cross marks the position of the nucleus, the white regions are masked locations where we were not able to fit the emission-line profiles, and the dotted lines represent the orientation of the line of nodes. The black contours in the residual map are from the 3-cm radio image with the same flux levels as shown in Fig. 2, and the white contours show radio contours at the 1.5σ level. The black asterisks labelled OH1 and OH2 mark the position of the maser sources.

Lawrence et al. (1999) described the construction of the QDOT survey, which consists of IR properties and redshifts of an all-sky sample of 2387 *IRAS* galaxies. They obtained a systemic velocity for IRAS F23199+0123 of 40 981 km s^{-1}. On the other hand, Darling & Giovanelli (2006) performed an optical spectrophotometric study of resolved spectra of multiple nuclei merging systems that hosts OHM sources and obtained $v_s = 40\,679 \pm 2$ km s^{-1}. We note that the systemic velocity derived here is smaller than those obtained in previous studies. We speculate that this difference may be due to the fact that previous works possibly have observed the western nucleus, which is brighter, since at that time it was not known that IRAS F23199+0123 is composed by two members.

Besides the disc rotation model, Fig. 8 shows also the observed Hα velocity field in the left-hand panel and the residual map between the observed velocities and the model in the right-hand panel. The residual velocity map shows values much smaller than the observed velocity amplitude, but residuals of up to 100 km s^{-1} are present at some locations. Blueshifts are seen to the south and north of the nucleus, while redshifts are observed at the nucleus and its surroundings.

In order to investigate the origin of the velocity residuals, we have overlaid the contours from the 3-cm radio image on the residual map shown in the right-hand panel of Fig. 8. In this figure, we have plotted also the radio contours at the 1.5σ level (in white), as these levels show that faint radio emission is elongated towards the region where blueshifts are observed to the north of the nucleus. At the 3σ level there is just a hint of this elongation. This apparent association of the extended radio emission (although at faint levels) with the blueshifts in the map of velocity residuals suggests that the radio-emitting plasma may play a role in the gas kinematics and a possible interpretation is that the blueshifted residuals are due gas pushed away from the nucleus by a radio jet. Other indications of the interaction between the radio plasma and the emitting gas are the higher velocity dispersion and [N II]/Hα values surrounding the radio structures, as seen in Figs 5 and 6. Similar results have been found for other galaxies and interpreted as originating from the interaction of the radio jet with the ambient gas (e.g. Riffel et al. 2006; Riffel, Storchi-Bergmann & Riffel 2015).

We speculate that the observed blueshifts originate in outflows along a bicone oriented in the north–south direction with its axis approximately in the plane of the sky. The blueshifts would come from the front walls (nearside) of the cones to both sides of the nucleus, while the redshifts from the back (farside) walls are not observed probably due to obscuration. The redshifts that are observed surrounding the nucleus could be due to inflows towards the nucleus, probably due to gas motions associated with the interaction between the two galaxies of the pair.

Finally, it is interesting to note that the OH masers are observed in the vicinity of the active nucleus of IRAS F23199E, close to regions of enhanced velocity dispersion and [N II]/Hα ratio in the emitting gas. This suggests that the maser sources are associated with the AGN, perhaps produced in gas compressed in an interaction with expanding radio plasma. We also notice that the redshifted maser source (OH1) is located in a region with redshifted residuals, while the blueshifted maser source (OH2) is located in a region of blueshifted residuals, suggesting that the OH2 source is participating in the outflow.

4.4 The nature of the nuclear emission

Darling & Giovanelli (2006) presented a study of the optical properties of the Arecibo Observatory OHM survey sample, with the aim of investigating the types of nuclear environments that produce OHMs. They determined that IRAS F23199+0123 harbours a Seyfert 2 nucleus, based on an optical spectrum but the spectra used for the classification includes both nuclei, thus it was not possible to reveal the nature of each nucleus separately.

With our data we have discovered that IRAS 23199E harbours a Seyfert 1 nucleus, as we clearly detected a broad unresolved Hα component at the nucleus and the WHAN diagram is consistent with Seyfert-like gas excitation there. The double-peaked nature of this broad component suggests it is due to unresolved disc rotation in the BLR, as many recent studies have supported a flattened geometry for this region (Storchi-Bergmann et al. 2017). In the narrow-line region (NLR), jet–cloud interaction may give rise to double-peaked lines (e.g. Capetti et al. 1999; O'Dea et al. 2002;

Kharb et al. 2017) and another possibility is that some interaction with the radio emission may be happening in the BLR in this particular case. The discrepancy between Darling's classification and ours can be understood if Darling & Giovanelli (2006) observed the western nucleus, which appears brighter in our *HST* image and in the Sloan Digital Sky Survey (SDSS) image (Bundy et al. 2015; Albareti et al. 2017).

We estimate the mass of the central black hole using the empirical relation given by Greene & Ho (2005):

$$\frac{M_{\rm BH}}{M_\odot} = (2.0^{+0.4}_{-0.3}) \times 10^6$$

$$\left(\frac{L_{\rm H\alpha}}{10^{42}\,{\rm erg\,s^{-1}}}\right)^{0.55\pm0.02} \left(\frac{{\rm FWHM}_{\rm H\alpha}}{10^3\,{\rm km\,s^{-1}}}\right)^{2.06\pm0.06}, \qquad (7)$$

where $M_{\rm BH}$ is the black hole mass, $L_{\rm H\alpha}$ is the luminosity, and FWHM$_{\rm H\alpha}$ is the full width at half-maximum of the broad component. The luminosity was calculated as the sum of the luminosities of both components, resulting in $L_{\rm H\alpha} \approx 1.8 \times 10^{41}\,{\rm erg\,s^{-1}}$. We obtained the FWHM$_{\rm H\alpha}$ of $2170\,{\rm km\,s^{-1}}$ directly from the observed profile. Using these values we have estimated a black hole mass of $3.8^{+0.3}_{-0.2} \times 10^6\,{\rm M_\odot}$.

5 CONCLUSIONS

We present a multiwavelength study of the OHM galaxy IRAS F23199+0123 using the *HST*, VLA, and Gemini North Telescope. Our *HST* images show that this system is an interacting pair of galaxies and used integral field spectroscopic data obtained with the GMOS-IFU to observe its eastern nucleus, which we call IRAS F23199E. Our observations cover the inner $9.5 \times 13\,{\rm kpc}^2$ of the galaxy at a spatial resolution of 2.3 kpc and velocity resolution of $\sim 70\,{\rm km\,s^{-1}}$. Our main conclusions are as follows.

(i) We show that IRAS F23199+0123 is an interacting pair with a tidal tail connecting the two galaxies and detect two OH maser sources associated with the eastern member.

(ii) Both nuclei present extended radio emission at 3 and 20 cm, with intensity peaks at the each nucleus. The 20 cm radio emission of the eastern nucleus is elongated in the direction of the most extended emission in the *HST* continuum image (north-east–south-west), while in the western nucleus the 20 cm radio emission is tilted by about 45° eastwards relative to the orientation of the most extended continuum emission. In the better spatially resolved 3-cm observations, some elongation is observed at low brightness level towards the north in the eastern nucleus.

(iii) One of the main results of this paper is the discovery of a Seyfert 1 nucleus in IRAS F23199E, via the detection of an unresolved broad (FWHM $\approx 2200\,{\rm km\,s^{-1}}$) double-peaked component in the Hα emission line from the BLR. This is important in regard to the OH maser emission, because the two masing sources are detected in this galaxy that hosts an AGN, rather than the other member of the pair. In addition, the masing sources are observed in the vicinity of enhanced velocity dispersion and higher line ratios, suggesting that they are associated with shocks driven by AGN outflows. The blue- and redshifted maser sources are associated with the blue- and redshifted ionized gas velocity residuals. This combination of evidence from *HST* images, VLA line spectroscopy, and IFU spectroscopy strongly indicates that in this system the OHM sources are associated with the AGN rather than star formation.

(iv) Using the width and luminosity of the broad Hα profile, we estimate a mass of $M_{\rm BH} = 3.8^{+0.3}_{-0.2} \times 10^6\,{\rm M_\odot}$ for the central supermassive black hole.

(v) The comparison between the *HST* [N II]+Hα image and GMOS-IFU emission-line flux distributions of IRAS F23199E shows that they are similar, being more elongated in the north-east–south-west direction, following the continuum emission. In addition, the GMOS Hα flux map reveals the presence of three extranuclear knots, attributed to star-forming regions.

(vi) From the measurement of the Hα fluxes from the star-forming regions, we obtain: (1) SFRs in the range (0.05–0.12) ${\rm M_\odot\,yr^{-1}}$; (2) ionized gas content in the range (1.8–4.1) $\times 10^5\,{\rm M_\odot}$; and (3) ionized photons rate log Q[H$^+$] = 51.9–52.2 s^{-1}. From the FIR luminosity we obtain SFR $\approx 61\,{\rm M_\odot\,yr^{-1}}$ suggesting that most of the FIR luminosity may be due to the AGN or due to star formation embedded in dust.

(vii) The [N II] $\lambda6583$/Hα flux ratio map of IRAS 23199E presents the highest values coincident with the regions with highest σ values, which surround the radio source and suggests that the radio-emitting plasma interacts with the ambient gas via shocks that seem to play a role in the gas excitation. The lowest [N II] $\lambda6583$/Hα values are cospatial with the star-forming regions detected in the Hα emission.

(viii) The velocity fields of IRAS F23199E show a disturbed rotation pattern with the line of nodes oriented along PA = 95°, as derived by the fit of the Hα velocities with a rotation disc model. The residuals between the observed and modelled velocity field combined with the velocity dispersion maps suggest the presence of non-circular motions, possibly due to outflows from the nucleus along the directions north and south and inflows towards the nucleus in its vicinity.

REFERENCES

Albareti F. D. et al., 2017, ApJS, 233, 25
Allington-Smith J. et al., 2002, PASP, 114, 892
Baldwin J. A., Phillips M. M., Terlevich R., 1981, PASP, 93, 5
Belfiore F. et al., 2016, MNRAS, 461, 3111
Bertola F., Bettoni D., Danziger J., Sadler E., Sparke L., de Zeeuw T., 1991, ApJ, 373, 369
Brum C., Riffel R. A., Storchi-Bergmann T., Robinson A., Schnorr Muller A., Lena D., 2017, MNRAS, 469, 3405
Bundy K. et al., 2015, ApJ, 798, 7

Capetti A., Axon D. J., Macchetto F. D., Marconi A., Winge C., 1999, ApJ, 518, 187

Cid Fernandes R., Stasinska G., Schlickmann M. S, Mateus A., Vale Asari N., Schoenell W., Sodre L., 2010, MNRAS, 403, 1036

Cid Fernandes R., Stasinska G., Mateus A., Vale Asari N., 2011, MNRAS, 413, 1687

Conway J. E., Cornwell T. J., Wilkinson P. N., 1990, MNRAS, 246, 490

Darling J., Giovanelli R., 2001, AJ, 121, 1278

Darling J., Giovanelli R., 2002, ApJ, 572, 810

Darling J., Giovanelli R., 2006, AJ, 132, 2596

Díaz Á. I., Terlevich E., Castellanos M., Hägele G. F., 2007, MNRAS, 382, 251

Dors O. L., Storchi-Bergmann T., Riffel R. A., Schmidt A. A., 2008, A&A, 482, 59

Falcón-Barroso J., Ramos Almeida C., Boker T., Schinnerer E., Knapen J. H., Lançon A., Ryder S., 2014, MNRAS, 438, 329

Galliano E., Alloin D., 2008, A&A, 487, 519

Gonzalez R. C., Woods R. E., 2002, Digital Image Processing, 2nd edn. Prentice-Hall, Englewood Cliffs, NJ

Greene J. E., Ho L. C., 2005, ApJ, 630, 122

Hook I., Jorgensen I., Allington-Smith J. R., Davies R. L., Metcalfe N., Murowinski R. G., Crampton D., 2004, PASP, 116, 425

Hoopes C. G., Walterbos R. A. M., Rand R. J., 1999, ApJ, 522, 669

Kennicutt R. C., 1998, ARA&A, 36, 189

Kharb P., Subramanian S., Vaddi S., Das M., Paragi Z., 2017, ApJ, 846, 12

Lawrence A. et al., 1999, MNRAS, 308, 897

Lena D., 2014, preprint (arXiv:1409.8264)

Lo K. Y., 2005, ARA&A, 43, 625

McMullin J. P., Waters B., Schiebel D., Young W., Golap K., 2007, in Shaw R. A., Hill F., Bell D. J., eds, ASP Conf. Ser. Vol. 376, Astronomical Data Analysis Software and Systems XVI. Astron. Soc. Pac., San Francisco, p. 127

Markwardt C. B., 2009, in Bohlender D. A., Durand D., Dowler P., eds, ASP Conf. Ser. Vol. 411, Astronomical Data Analysis Software and Systems XVIII. Astron. Soc. Pac., San Francisco, p. 251

Menezes R. B., Steiner J. E., Ricci T. V., 2014, MNRAS, 438, 2597

Menezes R. B., da Silva P., Ricci T. V., Steiner J. E., May D., Borges B. W., 2015, MNRAS, 450, 369

O'Dea C. P. et al., 2002, AJ, 123, 2333

Osterbrock D. E., 1989, Astrophysics of Gaseous Nebulae and Active Galactic Nuclei. University Science Books, Mill Valley, CA

Pearson T. J., Readhead A. C. S., 1984, ARA&A, 22, 97

Peterson B. M., 1997, An Introduction to Active Galactic Nuclei. Cambridge Univ. Press, Cambridge

Rau U., Cornwell T. J., 2011, A&A, 532, A71

Riffel R. A., 2010, Ap&SS, 327, 239

Riffel R. A., Storchi-Bergmann T., Winge C., Barbosa F. K. B., 2006, MNRAS, 373, 2

Riffel R. A., Storchi-Bergmann T., Dors O. L., Winge C., 2009, MNRAS, 393, 783

Riffel R. A., Storchi-Bergmann T., Riffel R., 2015, MNRAS, 451, 3587

Riffel R. A. et al., 2016, MNRAS, 461, 4192

Rossa J., Dettmar R.-J., 2000, A&A, 359, 433

Rossa J., Dettmar R.-J., 2003, A&A, 406, 505

Sales D. A. et al., 2015, ApJ, 799, 25

Schwab F. R., 1984, AJ, 89, 1076

Storchi-Bergmann T., Dors O. L., Jr, Riffel R. A., Fathi K., Axon D. J., Robinson A., Marconi A., Ostlin G., 2007, ApJ, 670, 959

Storchi-Bergmann T., Schimoia J. S., Peterson B. M., Elvis M., Denney K. D., Eracleous M., Nemmen R. S., 2017, ApJ, 835, 236

Tody D., 1986, in Crawford D. L., ed., Proc. SPIE Vol. 627, Instrumentation in Astronomy VI. SPIE, Bellingham, p. 733

Tody D., 1993, in Hanisch R. J., Brissenden R. J. V., Barnes J., eds, ASP Conf. Ser. Vol. 52, Astronomical Data Analysis Software and Systems II. Astron. Soc. Pac., San Francisco, p. 173

van der Kruit P. C., Allen R. J., 1978, ARA&A, 16, 103

van Dokkum P. G., 2001, PASP, 113, 1420

Wold M., Galliano E., 2006, MNRAS, 369, 47

This paper has been typeset from a TEX/LATEX file prepared by the author.